

Article

Revealing the Enhancement Mechanism of Laser Cutting on the Strength–Ductility Combination in Low Carbon Steel

Jie Chen , Feiyue Tu, Pengfei Wang and Yu Cao * 

Zhejiang Provincial Key Laboratory of Laser Processing Robotics, College of Mechanical & Electrical Engineering, Wenzhou University, Wenzhou 325035, China; chenjie@wzu.edu.cn (J.C.)

* Correspondence: yucao@wzu.edu.cn

Abstract: The strength–ductility mechanism of the low-carbon steels processed by laser cutting is investigated in this paper. A typical gradient-phased structure can be obtained near the laser cutting surface, which consists of a laser-remelted layer (LRL, with the microstructure of lath bainite + granular bainite) and heat-affected zone (HAZ). As the distance from the laser cutting surface increases, the content of lath martensite decreases in the HAZ, which is accompanied by a rise in the content of ferrite. Considering that the microstructures of the LRL and HAZ are completely different from the base metal (BM, ferrite + pearlite), a significant strain gradient can be inevitably generated by the remarkable microhardness differences in the gradient-phased structure. The hetero-deformation-induced strengthening and hardening will be produced, which is related to the pileups of the geometrically necessary dislocations (GNDs) that are generated to accommodate the strain gradient near interfaces. Plural phases of the HAZ can also contribute to the increment of the hetero-deformation-induced strengthening and hardening during deformation. Due to the gradient-phased structure, the low carbon steels under the process of laser cutting have a superior combination of strength and ductility as yield strength of ~487 MPa, tensile strength of ~655 MPa, and total elongation of ~32.7%.

Keywords: laser cutting; gradient-phased structure; strength–ductility synergy; geometrically necessary dislocation



Citation: Chen, J.; Tu, F.; Wang, P.; Cao, Y. Revealing the Enhancement Mechanism of Laser Cutting on the Strength–Ductility Combination in Low Carbon Steel. *Metals* **2024**, *14*, 541. <https://doi.org/10.3390/met14050541>

Academic Editor: Catalin Constantinescu

Received: 15 February 2024

Revised: 27 April 2024

Accepted: 29 April 2024

Published: 2 May 2024



Copyright: © 2024 by the authors. Licensee MDPI, Basel, Switzerland. This article is an open access article distributed under the terms and conditions of the Creative Commons Attribution (CC BY) license (<https://creativecommons.org/licenses/by/4.0/>).

1. Introduction

Electricity is inextricably linked to socio-economic development and people's livelihood. Unfortunately, about 700 million people still lack access to electricity in the world, according to estimations by the International Energy Agency [1]. Meanwhile, the production and consumption of electricity are unbalanced in many countries, generating a shortage or excess of electricity supply in some areas [2]. In order to transmit the electricity from the surplus regions to the deficient regions, a large amount of high voltage, extra high voltage, and ultra-high voltage power transmission projects are being constructed or under planning. Therefore, the demand for transmission towers increases significantly.

Generally, the low carbon steels after rolling with a yield strength ranging from ~235 MPa to ~420 MPa have been widely used in transmission towers, which, under the guidance of the rolling force model, guarantee superior strip flatness [3,4]. Considering the bolted connections of the transmission towers [5], the low carbon steels should be cut into specific sizes and then made into holes. For the blanking process, the laser cutting technique has replaced wire-electrode cutting, flame cutting, plasma arc cutting, and so on [6]. First of all, the cutting precision and cross-section quality of the laser cutting technique can satisfy the requirements of manufacturing the transmission towers [7,8]. According to the research of Andrés et al. [8], the laser cutting process can obtain relatively high precision among several thermal cutting technologies (such as flame cutting and plasma arc cutting). Secondly, the superb cutting performance of the laser cutting machine can effectively improve the production efficiency of the transmission towers [6]. Specifically,

the cutting speed of the 12 mm thickness carbon steel is 8500~9000 mm/min by the laser cutting machine with the maximal output power of 20 kW. Thirdly, the kerf width under the process of laser cutting is less than that of the flame cutting and plasma arc cutting [9,10], thus significantly reducing the loss of metallic materials. Finally, in contrast to the wide heat-affected zone (HAZ) induced by the continuously exothermal process of flame cutting [11], the HAZ of laser cutting is much narrower, which ascribes to its relatively low heat input [12,13]. The width of the HAZ in plasma arc cutting presents an intermediate situation [13].

Based on the above advantages of the laser cutting technique, more and more transmission tower manufacturers are attempting to adopt the laser cutting machine to make holes in the steel plates; thus, the drilling and punching machines will be replaced. In other words, the blanking and hole-making processes can be completed only by a laser cutting machine, which shortens the manufacturing process, as well as the cost. However, it remains a challenge to manufacture qualified transmission towers by the process of laser hole-making [13]. This is mainly because of the effect of the heat affected zone (HAZ) generated by the laser cutting process on the strength–ductility combination and the fact that its deformation mechanisms remain unsolved [8,14–16], whereas the bolt holes produced by the drilling and punching machines do not have the HAZ. Specifically, most studies relative to the laser-cutting process of low-carbon steels have focused on the relationship between laser cutting parameters, cutting accuracy, and cutting section quality [14–18]. Almost no studies have clarified the strength–ductility evolution mechanism induced by HAZ near the laser cutting surface, although some researchers carried out tensile property tests [13,19].

Therefore, this paper studies the strength and ductility mechanisms of the low carbon steel under the process of laser cutting, which are the two baseline mechanical properties of the transmission towers. Based on the analysis of microstructural evolution induced by laser cutting, the relationships between gradient-phased structure and tensile properties are discussed in detail and the mechanism of the enhanced strength–ductility combination by the laser cutting process will be clarified.

2. Experimental Procedures

2.1. Material

The chemical composition of the experimental steel (designated as Q420 in China, which belongs to low carbon low alloy steel) is shown in Table 1. After hot rolling, the yield strength of the ~30 mm thickness low carbon steel plates is ~420 MPa.

Table 1. Chemical composition of the experimental steels, wt.%.

C	Si	Mn	Cr	Mo	Ni	Co
0.13	0.10	1.56	0.04	0.05	0.05	0.008

2.2. Laser Cutting Processes

In order to study the effect of microstructural evolution induced by laser cutting on the strength–ductility combination of the low carbon steels, hot-rolled steel plates with a length of ~90 mm were cut into slices of ~8 mm thickness by the laser cutting machine, as illustrated in Figure 1. Specifically, the laser cutting head moved along the length direction at a speed of ~800 mm/min and the intense energy of the focused laser beam caused the irradiated area of the low-carbon steel plates to melt or vaporize, after which high-pressure gas removed the molten metals, the technological parameters of the laser cutting process are listed in Table 2. The parameter setting of the laser cutting process is obtained based on practical industrial production, which mainly depends on the grade and thickness of the steel.

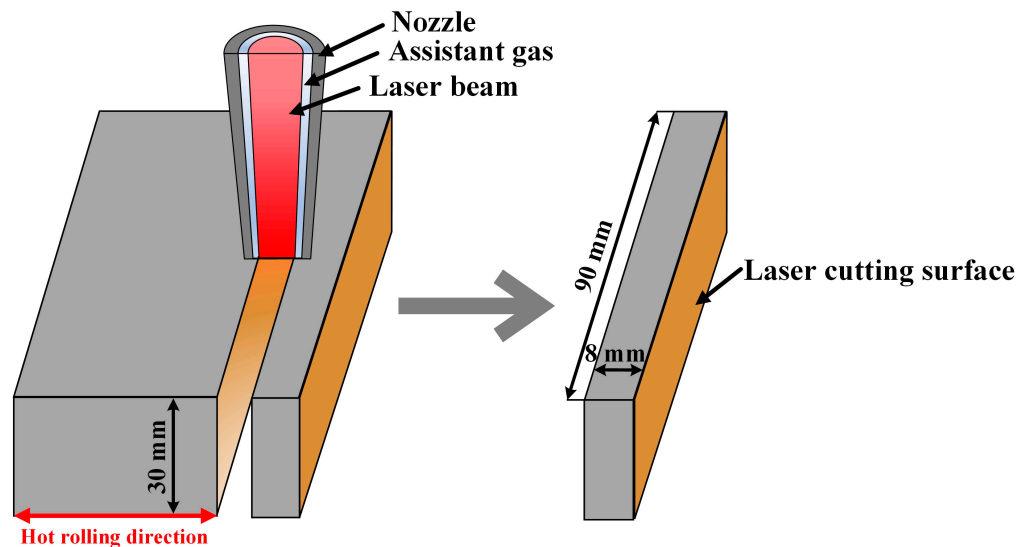


Figure 1. Schematic illustration of the laser cutting process.

Table 2. Technological parameters for laser cutting of the experimental steel.

Parameter	Value	Parameter	Value
Operating condition	Continuous/fiber	Focal length (mm)	250
Wavelength (nm)	1060	Assistant gas (purity)	Oxygen ($\geq 99.5\%$)
Cutting speed (mm/min)	800	Assistant gas pressure (bar)	0.8
Laser power (kW)	15	Focus diameter (mm)	0.04
Defocusing distance (mm)	-20	Type of nozzle	conical

2.3. Microstructural Characterization

Metallographic specimens were cut from the experimental materials that were processed by laser cutting. After mechanical polishing and etching with $\sim 4\%$ initial solution, the cross-sectional microstructures of the specimens were characterized using an OLYMPUS BX53M optical microscope (OM) (OLYMPUS, Tokyo, Japan) and a Hitachi SU8010 field-emission scanning electron microscope (SEM) (Hitachi, Tokyo, Japan). For the electron backscatter diffraction (EBSD) analysis, the specimens were electropolished by an electrolyte that consisted of ~ 12.5 vol.% perchloric acid and ~ 87.5 vol.% ethyl alcohol with the potential of ~ 25 V for ~ 20 s. A scanning step of ~ 0.2 μm was carried out for the EBSD analysis and the acquired data were post-processed by AztecCrystal software (<https://nano.oxinst.com/azteccrystal>, accessed on 28 April 2024) to diminish the point of zero solutions.

2.4. Mechanical Properties Evaluation

The uniaxial tensile tests of the dog-bone-shaped specimens were conducted using an Instron 3369 universal testing machine which is equipped with a non-contacting video extensometer. The sheet-typed tensile specimens possessed a gauge length of ~ 25 mm and were measured at a strain rate of $\sim 2 \times 10^{-3} \text{ s}^{-1}$ under room temperature. In order to reveal the influence of laser cutting on the strength and ductility, three types of specimens were tested. The first one was the specimens that had two laser-cutting surfaces, as shown in Figure 2a. In other words, the thickness of the first tensile specimen was ~ 8 mm, which was in accordance with the thickness of the laser-cut slices in Figure 1. According to Figure 2b, the second tensile specimen with a thickness of ~ 1 mm only contained the laser-cutting surface and the third tensile specimen was cut from the central region of the laser-cut slices. The thickness of the third tensile specimen was the same as that of the second one. For convenience, the first tensile specimen, which contained the entire laser-cut slices, could be denoted as ELCS. By analogy, the second and third tensile specimens were referred to

as SLCS (superficial laser-cut slices) and CLCS (central laser-cut slices), respectively. To ensure the measuring accuracy, the average of the three tensile test results was recorded as the value for the corresponding specimens. The microhardness distributions of the cross-section, which was perpendicular to the laser cutting surface, could be obtained by the HXD-1000TM/LCD microhardness tester under the load of ~ 9.8 N with a holding time of ~ 15 s.

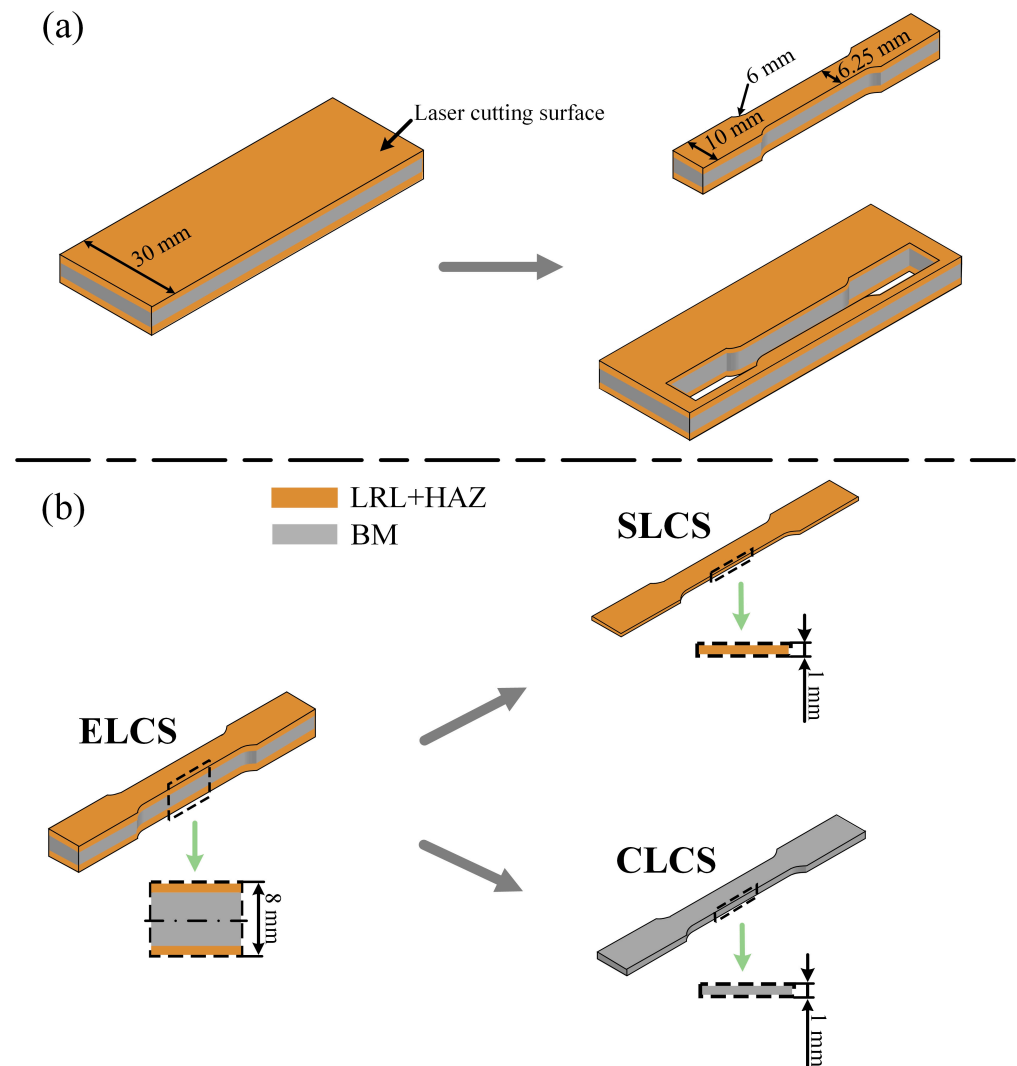


Figure 2. The sampling methods of the three kinds of tensile specimens. (a) A schematic diagram of the machining of the ELCS specimen and (b) sampling positions of the SLCS and CLCS specimens.

3. Results and Discussion

3.1. Microstructural Evolution

The OM and SEM observations of the experimental steels processed by laser cutting are shown in Figure 3. Obviously, the thermal effect, which is induced by the laser cutting process, can lead to phase transformation, according to Figure 3a. Specifically, the microstructure near the laser cutting surface is totally different from the base metal (BM) and it can be divided into laser remelted layer (LRL) and HAZ. Based on the relatively narrow phase transformation region with a width of ~ 0.9 mm in Figure 3a, it may be easily deduced that the depth of the HAZ under the process of laser cutting is narrower than that of the other thermal cutting methods, such as flame cutting, plasma arc cutting, and so on [20,21]. This may be ascribed to the high energy density of the laser beam and high cutting speed of the laser cutting, leading to less heat input [13].

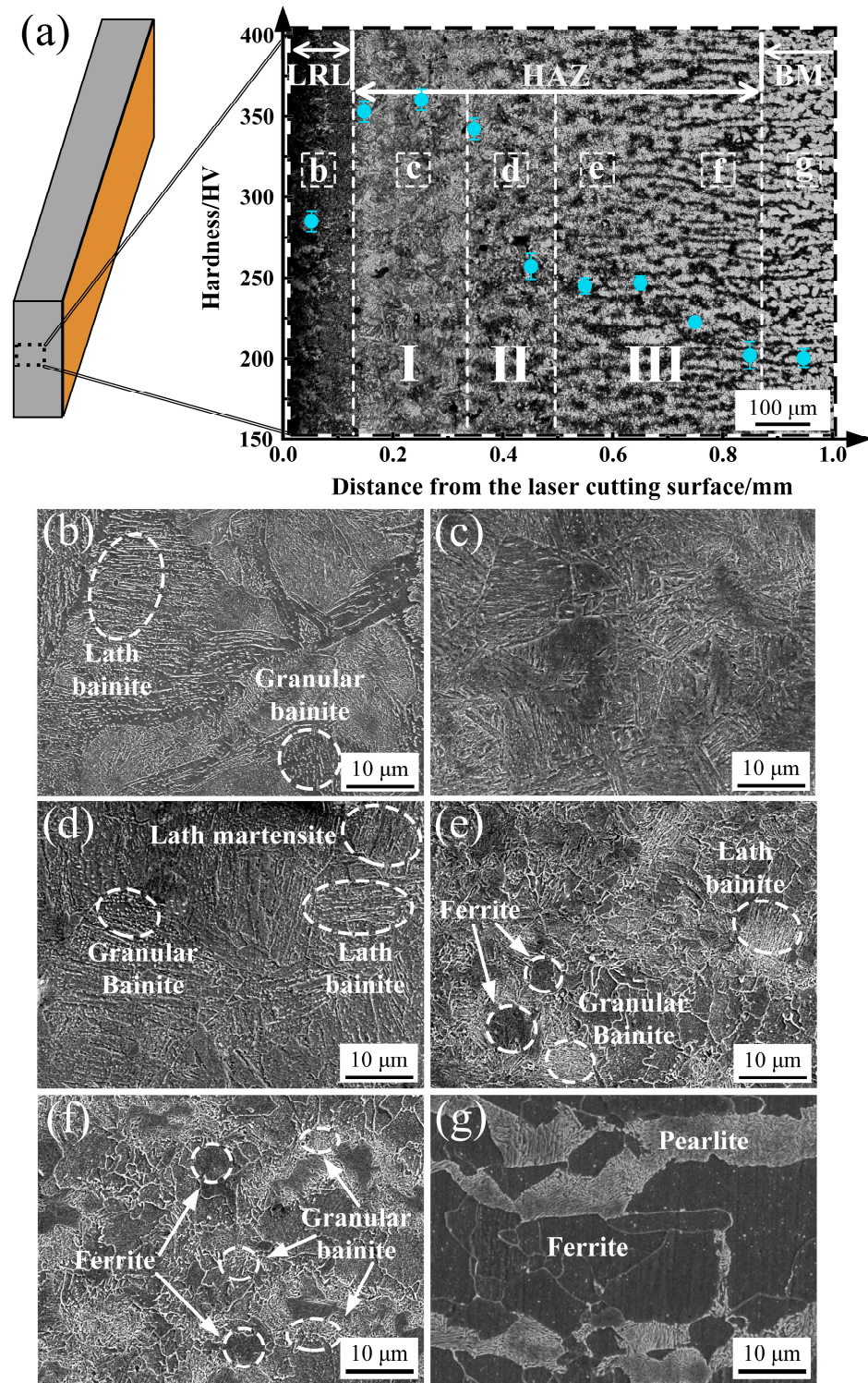


Figure 3. Microstructure of the low carbon steel near the laser cutting surface. (a) Metallographic structure and microhardness distribution within the depth of ~1.0 mm; (b) SEM image of the LRL; (c–f) SEM images of the HAZ; and (g) SEM image of the BM.

In order to study the microstructural evolution induced by the laser cutting, the microscopic morphologies of the LRL and HAZ are presented in Figure 3b–g. It is shown in Figure 3b that the microstructure of the LRL is mainly made up of lath bainite and granular bainite. The HAZ can be divided into three layers, due to the significantly different microstructure of each layer. Typical martensite with lath morphology can be

observed in the outermost layer of the HAZ (layer I), as shown in Figure 3c. Generally, the prior austenite grains consist of several packets, which have the same habit plane, and the packets are composed of one or two blocks [22]. Moreover, many laths with low-angle grain boundaries exist within each block. Therefore, the hierarchical structure of lath martensite contributes to microstructure refinement, which produces the supreme microhardness of ~363 HV. A complex microstructure with lath martensite, lath bainite, and granular bainite can be found in layer II of the HAZ, as shown in Figure 3d. As the depth from the laser cutting surface increases, the lath martensite gradually vanishes along with the emergence of ferrite, according to Figure 3e,f. Compared to layer I, the relatively low microhardness in layers II and III is primarily caused by the decreased content of lath martensite. In particular, the microhardness of layer III with few lath martensite decreases dramatically. For the BM, the ferrite and pearlite phase transformation occurs under the process of hot-rolling with subsequent air-cooling. Meanwhile, the flat grains of the BM elongate along the rolling direction.

During the process of laser cutting, the high peak temperature and uneven cooling rate are generated, which together produce the gradient-phased structure near the laser cutting surface of the low-carbon steel. Figure 4 shows the schematic representation of the formation of martensite and bainite at various depths. The irradiated steel plates will be melted or gasified by the focused laser beam with high energy density. Despite the fact that most of the molten metal would be removed by the assistant gas with high pressure, some molten metal may be kept at the laser cutting surface. As a result, the LRL with the microstructure of lath bainite and granular bainite can be obtained. On the one hand, the narrow kerf of laser cutting decreases the volume of the molten pool, resulting in a relatively quick cooling rate, which makes it difficult to detect ferrite and pearlite. On the other hand, the cooling rate of LRL fails to reach the critical cooling rate of martensitic transformation. This can be mainly attributed to the relatively poor efficiency of heat conduction induced by the pores between the LRL and HAZ [23], as well as the removal of the assistant gas when the LRL cools to the temperature of bainite transformation.

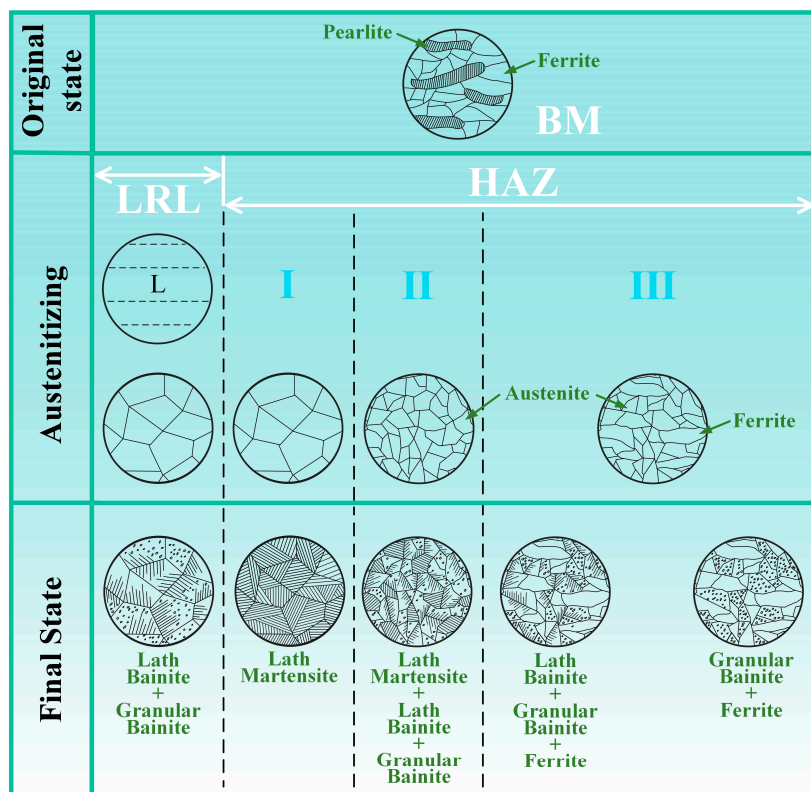


Figure 4. Schematic illustrations of the microstructural evolution during the laser cutting.

The peak temperature gradually decreases along with the increase in the depth from the laser cutting surface, which is similar to the characteristics of the welding thermal cycle [24,25]. Considering that the relatively high peak temperature occurs at the position near the laser cutting surface [26], the prior austenite grain size of layer I is greater than the other regions of the HAZ. On the contrary, part of the ferrite and pearlite transform to the austenite in layer III. Subsequently, this comparatively coarse austenite transforms to the lath martensite due to the superior heat transfer rates by the large temperature difference between layer I and BM, coupled with the cooling effect of assistant gas. As the distance from the laser cutting surface continues to increase, the cooling rate of the HAZ will decline. Therefore, the lath martensite can be hardly obtained, whereas the lath bainite and granular bainite exist.

3.2. Mechanical Property

The tensile engineering stress–strain behaviors of the SCLS, ELCS, and CLCS samples are shown in Figure 5a and the corresponding true stress–strain curves are also shown in Figure 5b. The squares in Figure 5a,b mark the start of necking according to the Considère criterion. In general, there is a gradual decline in the yield strength and tensile strength of the samples as the volume fraction of the BM increases. The SCLS sample shows the highest tensile strength of ~799 MPa with sacrificing tensile ductility. In contrast, the uniform elongation of the CLCS sample (~13.11%) is remarkably higher than the SLCS sample (~7.88%), accompanied by a significant drop in strength (tensile strength is ~559 MPa). Compared to the SCLS and CLCS samples, the ELCS sample exhibits a combination of high strength and good ductility (yield strength, tensile strength, and uniform elongation are ~487 MPa, ~655 MPa, and ~11.91%, respectively), which indicates that the gradient-phased structure induced by the laser cutting process can overcome the strength–ductility trade-off.

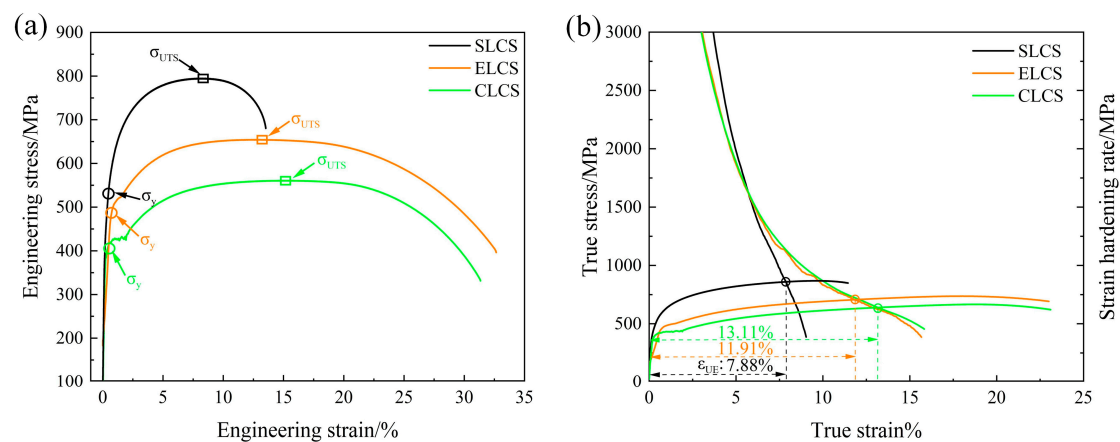


Figure 5. Mechanical properties of the SLCS, ELCS, and CLCS samples. (a) Engineering stress–strain curves and (b) true stress–strain curves versus corresponding strain hardening rate to estimate their uniform elongation.

To reveal the strain hardening capability of these three samples, the strain hardening rate versus true strain derived from Figure 5b is presented in Figure 6a. By increasing the strain, the overall strain hardening rates of these samples exhibit a similar decreasing trend. Obviously, the strain hardening rate of the SLCS sample presents the lowest rate of decline among these three samples during the early stage of deformation, which benefits from the extensive interactions between dislocations of lath martensite [27]. Owing to the insufficient mobile dislocations at the initial stage of deformation, the strain hardening rate curve of the ELCS and CLCS samples drops steeper than that of the SLCS sample [28–30]. At the later stage of tensile deformation, however, the SLCS sample exhibits a sharp drop in strain hardening rate. Considering that the high strain hardening rate can help retain the ductility, the relatively poor total elongation of the SLCS sample is ascribed to the plastic

instability caused by the low strain hardening rate [30]. Notably, an exceptional upturn phenomenon can be observed at a true strain of 1~2% for the ELCS and CLCS samples, as shown in Figure 6b,c. Upon reaching the yield stage, the dislocations quickly multiply and interact with each other to accommodate the applied strain, resulting in the non-monotonic strain hardening behavior in the ELCS and CLCS samples [31]. Compared to the CLCS sample, the ELCS sample possesses a comparatively higher strain hardening rate at the true strain of 1.6%–2.5%, which infers that the gradient-phased structure can generate more dislocations. By further increasing the tensile strain, no significant difference in the strain hardening rate curve between the ELCS and SLCS samples can be found, leading to the good ductility of the ELCS sample.

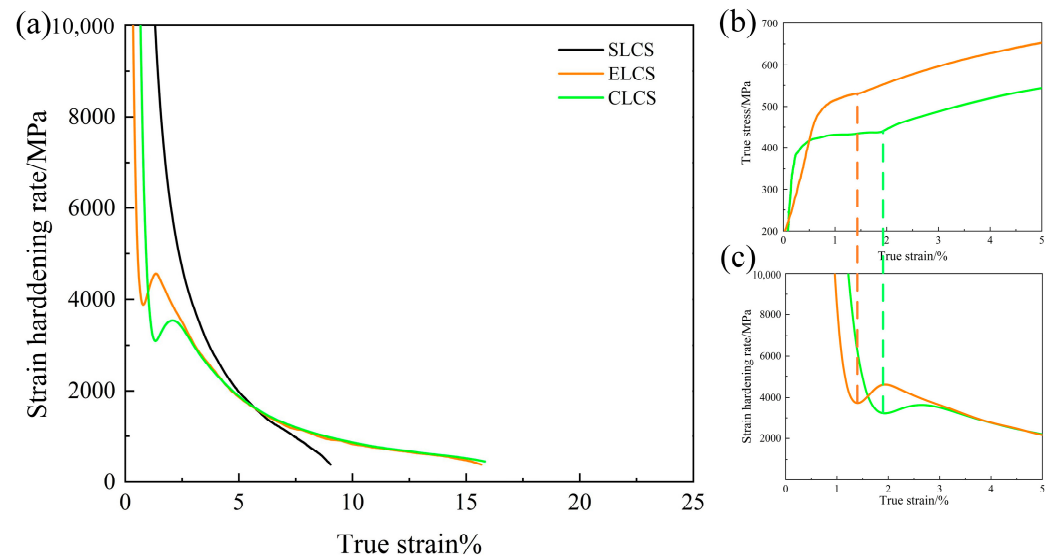


Figure 6. Strain hardening behavior of the SLCS, ELCS, and CLCS samples. (a) Variation in strain hardening rate with respect to true strain; (b) enlarged portion of the true stress–strain curves; and (c) enlarged portion corresponding to the strain hardening rate curves (the dash lines represent the upturn of the strain hardening rate).

3.3. Strength–Ductility Mechanisms of Gradient-Phased Structure

According to the above microstructural observations and tensile tests, laser cutting creates a typical gradient-phased structure with the characterization of central BM sandwiched by the LRL and HAZ, which aids in enhancing strength with retaining ductility. Figure 7 shows the distribution characteristics of microhardness along the direction of depth. The corresponding microhardness profile of the ELCS sample before tensile deformation reveals that the microhardness increases slightly from ~284 HV in the LRL layer to ~348 HV in the layer I of the HAZ, then decreases gradually with increasing distance from the laser cutting surface, and finally approaches to that of the BM counterpart (~201 HV) at the depth of ~1.0 μm . Clearly, the gradient distribution in microhardness originated from the gradient-phased structure obtained by laser cutting. After uniaxial tensile deformation, each layer of the ELCS sample shows a totally different change in the microhardness, whereas the increment of microhardness is undifferentiated throughout the entire thickness of the CLCS sample. Meanwhile, the increment curve of the microhardness for the SLCS sample exhibits a fluctuating changing trend, which is similar to that of the ELCS sample. Compared to the SLCS sample, it is worth noting that the difference in microhardness before and after tensile deformation in the ELCS sample is relatively larger. Such an obvious microhardness difference between the outer and inner layers in the ELCS sample will inevitably result in significant strain inhomogeneity during the process of tensile deformation.

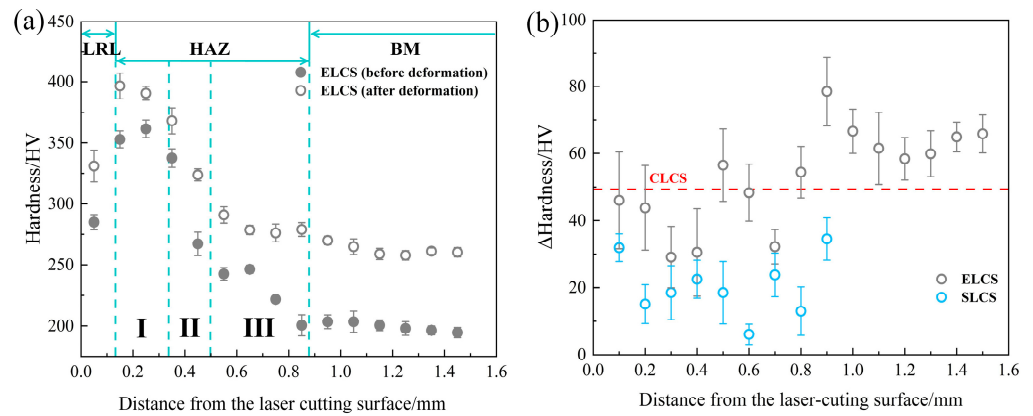


Figure 7. Microhardness distributions of the SLCS, ELCS, and CLCS samples. (a) Microhardness profiles corresponding to the depth of the ELCS sample and (b) variations of the microhardness before and after tensile deformation at various depths.

During the plastic deformation of the ELCS sample, the strain gradient, which is induced by the remarkable microhardness discrepancy of the gradient-phased structure, will be accommodated by pileups of the geometrically necessary dislocations (GNDs) to maintain the continuity of the interfaces [31–33]. To visually observe the evolution of geometrically necessary dislocations, the kernel average misorientation (KAM) map is used to calculate the GND density according to the EBSD data. In order to clarify the evolution mechanism of the GND for the gradient-phased structure, a homogeneous structure characterized by the microstructure of BM (denoted as BM sample) with a thickness of ~8 mm is selected as a control group and the KAM maps along the depth of ELCS sample and BM sample are shown in Figure 8. Generally, the GND density (ρ_{GND}) can be expressed by the following equation [34,35]:

$$\rho_{\text{GND}} = \frac{2\theta}{ub} \tag{1}$$

where θ is the average local misorientation calculated by the misorientation between a measurement point and its neighbor points [36], u represents the unit length of 0.2 μm , and b is the Burger’s vector. The KAM values exceeding the predefined threshold of 2° are excluded from the calculation since these points are considered as adjacent grains or subgrains instead of the accumulation of GNDs [36]. Therefore, the corresponding calculations of the GNDs density for the ELCS sample can be exhibited in Figure 9.

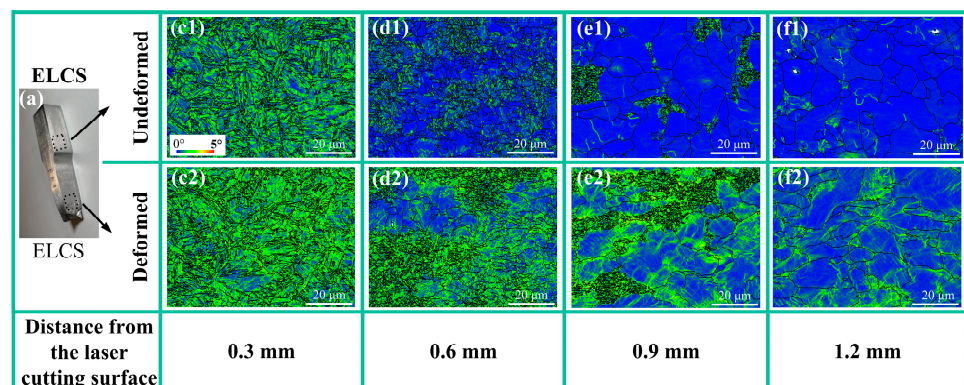


Figure 8. Cont.

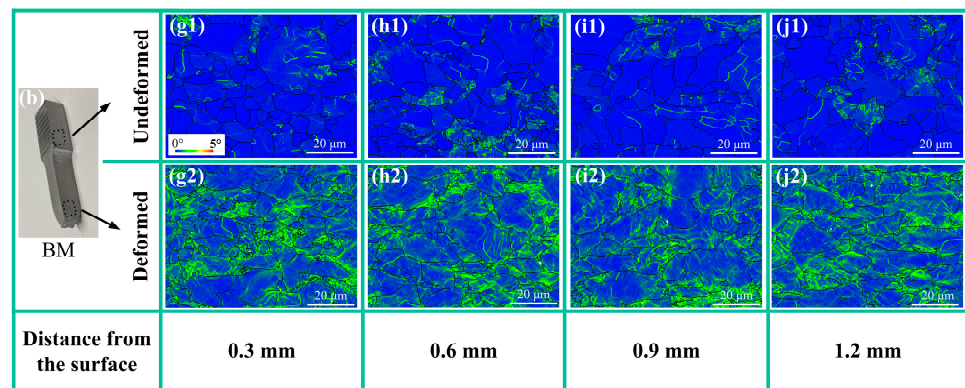


Figure 8. KAM mappings of the ELCS sample and BM sample at various depths (a,b) are a schematic diagram of the selected areas for the KAM analysis, (c1–j1) are obtained at the grip section, and (c2–j2) are obtained near the tensile fracture); (c1,c2,g1,g2) at a distance from the laser cutting surface of ~ 0.3 mm; (d1,d2,h1,h2) at a distance from the laser cutting surface of ~ 0.6 mm; (e1,e2,i1,i2) at a distance from the laser cutting surface of ~ 0.9 mm; and (f1,f2,j1,j2) are at a distance from the laser cutting surface of ~ 1.2 mm.

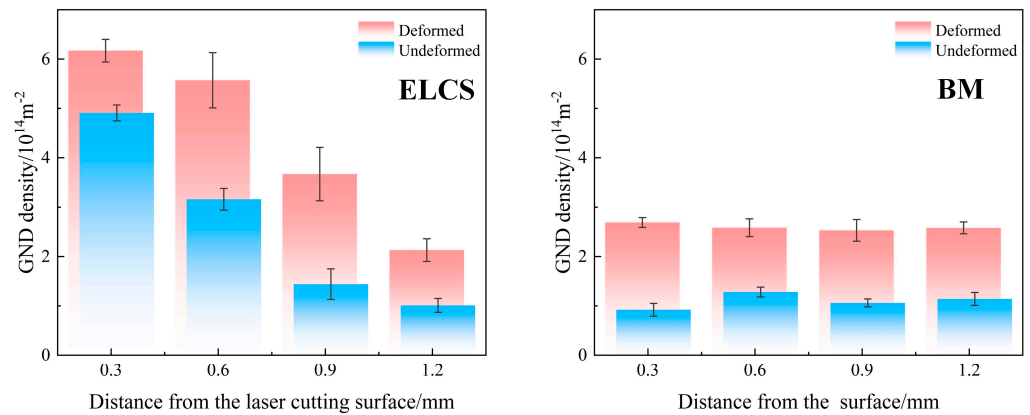


Figure 9. Variation in the GND density derived from the KAM value before and after deformation for the ELCS and BM samples.

Based on the distribution characteristics of the KAM value, the GND density at various depths is observed to be fundamentally different in the ELCS sample. The increase in GND density is relatively low when the distance from the laser cutting surface is ~ 0.3 mm, indicating that the lath martensite with higher yield strength may produce fewer plastic strains and accordingly lower growth of GND density during the process of tensile deformation. Considering that the soft ferrite + pearlite at the depth of ~ 1.2 mm needs to deform together with the hard lath martensite at the depth of ~ 0.3 mm, the BM (soft zone) thus cannot plastically deform freely [32,37]. In other words, the typical gradient-phased structure constrains the deformation of the soft ferrite + pearlite, which limits the increase in GND density in the BM, as evidenced by Figure 9. Surprisingly, the GNDs induced by the tensile deformation significantly increase in the layer at the depths from ~ 0.6 mm to ~ 0.9 mm. Since the strength/microhardness of the BM is lower than that of the layer I in the HAZ with the microstructure of hard lath martensite, the BM will start deforming plastically first, while the hard layer I remains deforming elastically at this stage [32]. The distinct deformation states between these two layers lead to the formation of the elastic–plastic interface, which mainly concentrates in the layers between layer I and BM [38]. Along with the increased strain, the elastic–plastic interface moves gradually from the position near the BM to the position near the layer I [39]. During the migration of the elastic–plastic interface, more GNDs will be generated and accumulated at the elastic–plastic interface constantly to maintain the continuity of the nearby layers. Meanwhile, compared to the

hard lath martensite with a large number of pre-existing dislocations, the lath bainite and granular bainite, which exist at the layers with depths from ~ 0.6 mm to ~ 0.9 mm, will remarkably enhance the ability of strain hardening. Therefore, the suitable bainitic microstructure with the improved ability of strain hardening contributes to the significant increase in GNDs at depths of ~ 0.6 mm and ~ 0.9 mm, as well as the elastic–plastic interface, which provides the space to allow the pile-up of GNDs. Furthermore, the accumulation of GNDs at the interface between the hard zone of lath martensite and the soft zone of ferrite + pearlite is generated to accommodate the strain gradient, producing forward stress in the hard zone and back stress in the soft zone, which together produce hetero-deformation-induced strengthening and hardening that enhance the strength and ductility of the gradient-phased structure [22,40]. Moreover, it should be noted that the GND density distribution of the HAZ at depths of ~ 0.6 mm and ~ 0.9 mm (as Figure 8(d2,e2) show) is also significantly heterogeneous. Due to the great variation in the strength between ferrite and bainite, the difference in the GND density evolution between them can be significant during deformation. Hence, the heterogenous-distributed GNDs of the HAZ can improve the hetero-deformation-induced strengthening and hardening as well [32], leading to a better strength–ductility combination of the ELCS sample. That is, the internal local hydrostatic stress caused by the plural phases of HAZ during deformation can also contribute to the improvement in the tensile property.

Hence, it may be easily deduced that the laser cutting process can effectively improve the tensile properties of the low-carbon steels. Consequently, laser cutting may be recommended as a promising technology for making bolt holes. Thereby, the blanking and drilling processes of the transmission towers can be accomplished by laser cutting technology, which greatly improves production efficiency, reduces the number of fabricating equipment, and lowers the manufacturing cost.

4. Conclusions

In the present study, the hot-rolled low-carbon steel plates were cut into slices of ~ 8 mm thickness by using the 15 kW fiber laser in order to study the thermal effect induced by the laser cutting on the tensile property. The microstructure evolution near the laser cutting surface and strength–ductility mechanisms are discussed in detail.

- The phase-transformed zone caused by the laser cutting is mainly composed of LRL and HAZ. The formation of lath bainite and granular bainite in the LRL is ascribed to the poor efficiency of heat conduction and removal of the assistant gas, which is derived from the survived molten metal. In the HAZ, lath martensite with the highest microhardness of ~ 363 HV exists in layer I; a complex microstructure consisting of lath martensite, lath bainite, and granular bainite is obtained in layer II, while the ferrite is substituted for the lath martensite in layer III. As a result, a typical gradient-phased structure can be acquired through the laser-cutting process;
- The ELCS sample has a desirable synergy of high strength and good ductility, compared to the SCLS and CLCS samples. Although the strain hardening rate of the ELCS sample drops steeper than the SLCS sample due to the insufficient mobile dislocations at the initial stage of deformation, the strain hardening rate shows an exceptional upturn at the true strain of 1–2% in the ELCS, which can be attributed to the rapid multiplication and interaction of the dislocations upon yielding. As the tensile strain further increases, the strain hardening rate of the ELCS sample is comparable to that of the SLCS sample, which has excellent ductility with sacrificing the strength;
- During tensile deformation of the gradient-phased structure, each layer with different microstructure deforms inhomogeneously, generating a significant strain gradient, which should be accommodated by the ultrahigh density of GNDs at the interfaces between the hard lath martensite in the layer I of the HAZ and the soft ferrite + pearlite in the BM. Therefore, the hetero-deformation-induced strengthening and hardening originating from the gradient-phased structure contribute to the extraordinary strength and ductility of the low-carbon steel plates under the process of laser cutting. Moreover,

heterogeneous-distributed GNDs density caused by plural phases of the HAZ during deformation can also contribute to the improvement in the tensile property of the ELCS sample;

- The optimal strength–ductility synergy of the ELCS sample indicates that laser cutting might be considered as an ideal technology to process the bolt holes of the electrical transmission tower.

Author Contributions: Conceptualization, J.C. and Y.C.; investigation, J.C., F.T., P.W. and Y.C.; writing—original draft preparation, F.T. and P.W.; writing—review and editing, J.C.; supervision, Y.C.; project administration, J.C. and Y.C.; funding acquisition, J.C. All authors have read and agreed to the published version of the manuscript.

Funding: This research was supported by the Zhejiang Provincial Natural Science Foundation of China under Grant No. LQ22E040001 and the Wenzhou Science and Technology Project under Grant Nos. ZG2022021 and ZG2023019.

Data Availability Statement: The data presented in this study are available on request from the corresponding author.

Conflicts of Interest: The authors declare no conflicts of interest.

References

1. Ortega-Arriaga, P.; Babacan, O.; Nelson, J.; Gambhir, A. Grid versus off-grid electricity access options: A review on the economic and environmental impacts. *Renew. Sustain. Energy Rev.* **2021**, *143*, 110864. [[CrossRef](#)]
2. Li, W.B.; Yang, M.Y.; Long, R.Y.; He, Z.X.; Zhang, L.L.; Chen, F.Y. Assessment of greenhouse gasses and air pollutant emissions embodied in cross-province electricity trade in China. *Resour. Conserv. Recycl.* **2021**, *171*, 105623. [[CrossRef](#)]
3. Zhang, S.H.; Deng, L.; Che, L.Z. An integrated model of rolling force for extra-thick plate by combining theoretical model and neural network model. *J. Manuf. Process.* **2022**, *75*, 100–109. [[CrossRef](#)]
4. Zhang, S.H.; Deng, L.; Tian, W.H.; Che, L.Z.; Li, Y. Deduction of a quadratic velocity field and its application to rolling force of extra-thick plate. *Comput. Math. Appl.* **2022**, *109*, 58–73. [[CrossRef](#)]
5. Bhowmik, C.; Chakraborti, P. Analytical and experimental modal analysis of electrical transmission tower to study the dynamic characteristics and behaviors. *Ksce J. Civ. Eng.* **2020**, *24*, 931–942. [[CrossRef](#)]
6. Tamura, K.; Ishigami, R.; Yamagishi, R. Laser cutting of thick steel plates and simulated steel components using a 30 kW fiber laser. *J. Nucl. Sci. Technol.* **2016**, *53*, 916–920. [[CrossRef](#)]
7. Pandey, A.K.; Dubey, A.K. Multiple quality optimization in laser cutting of difficult-to-laser-cut material using grey-fuzzy methodology. *Int. J. Adv. Manuf. Technol.* **2013**, *65*, 421–431. [[CrossRef](#)]
8. Cicero, S.; Garcia, T.; Alvarez, J.A.; Martin-Meizoso, A.; Aldazabal, J.; Bannister, A.; Klimpel, A. Definition and validation of Eurocode 3 FAT classes for structural steels containing oxy-fuel, plasma and laser cut holes. *Int. J. Fatigue* **2016**, *87*, 50–58. [[CrossRef](#)]
9. Cekic, A.; Begic-Hajdarevic, D.; Kulenovic, M.; Omerspahic, A. CO₂ laser cutting of alloy steels using N₂ assist gas. *Procedia Eng.* **2014**, *69*, 310–315. [[CrossRef](#)]
10. Dubey, A.K.; Yadava, V. Laser beam machining—A review. *Int. J. Mach. Tools Manuf.* **2008**, *48*, 609–628. [[CrossRef](#)]
11. Jokiahho, T.; Laitinen, A.; Santa-aho, S.; Isakov, M.; Peura, P.; Saarinen, T.; Lehtovaara, A.; Vippola, M. Characterization of Flame Cut Heavy Steel: Modeling of Temperature History and Residual Stress Formation. *Metall. Mater. Trans. B* **2017**, *48*, 2891–2901. [[CrossRef](#)]
12. Nyon, K.Y.; Nyeoh, C.Y.; Mokhtar, M.; Abdul-Rahman, R. Finite element analysis of laser inert gas cutting on Inconel 718. *Int. J. Adv. Manuf. Technol.* **2012**, *60*, 995–1007. [[CrossRef](#)]
13. Andres, D.; Garcia, T.; Cicero, S.; Lacalle, R.; Alvarez, J.A.; Martin-Meizoso, A.; Aldazabal, J.; Bannister, A.; Klimpel, A. Characterization of heat affected zones produced by thermal cutting processes by means of Small Punch tests. *Mater. Charact.* **2016**, *119*, 55–64. [[CrossRef](#)]
14. Boujelbene, M. Influence of the CO₂ laser cutting process parameters on the Quadratic Mean Roughness R_q of the low carbon steel. *Procedia Manuf.* **2018**, *20*, 259–264. [[CrossRef](#)]
15. Orshich, A.M.; Shulyatyev, V.B.; Golyshev, A.A. The Utmost Thickness of the Cut Sheet for the Qualitative Oxygen-assisted Laser Cutting of Low-carbon Steel. *Phys. Procedia* **2016**, *83*, 296–301. [[CrossRef](#)]
16. Pfeifer, R.; Herzog, D.; Hustedt, M.; Barcikowski, S. Pulsed Nd:YAG laser cutting of NiTi shape memory alloys—Influence of process parameters. *J. Mater. Process. Technol.* **2010**, *210*, 1918–1925. [[CrossRef](#)]
17. Naresh; Khatak, P. Laser cutting technique: A literature review. *Mater. Today Proc.* **2022**, *56*, 2484–2489. [[CrossRef](#)]
18. Li, M. Evaluation of the effect of process parameters on the cut quality in fiber laser cutting of duplex stainless steel using response surface method (RSM). *Infrared Phys. Technol.* **2021**, *118*, 103896. [[CrossRef](#)]

19. Ullah, S.; Li, X.Q.; Guo, G.Q.; Rodríguez, A.R.; Li, D.S.; Du, J.N.; Cui, L.; Wei, L.N.; Liu, X.C. Influence of the fiber laser cutting parameters on the mechanical properties and cut-edge microfeatures of a AA2B06-T4 aluminum alloy. *Opt. Laser Technol.* **2022**, *156*, 108395. [[CrossRef](#)]
20. Celik, Y.H. Investigating the Effects of Cutting Parameters on Materials Cut in CNC Plasma. *Mater. Manuf. Process.* **2013**, *28*, 1053–1060. [[CrossRef](#)]
21. Jokiahho, T.; Santa-Aho, S.; Peura, P.; Vippola, M. Cracking and Failure Characteristics of Flame Cut Thick Steel Plates. *Metall. Mater. Trans. A Phys. Metall. Mater. Sci.* **2020**, *51*, 1744–1754. [[CrossRef](#)]
22. Chen, J.; Li, C.S.; Chen, L.Q.; Fang, L.; Huo, S.B. Controlling of reheated quenching temperature of 1000 MPa grade steel plate for hydropower station. *Materwiss. Werksttech.* **2019**, *50*, 33–43. [[CrossRef](#)]
23. Yoon, S.; Han, G.D.; Jang, D.Y.; Kim, J.W.; Kim, D.H.; Shim, J.H. Fabrication of yttria-stabilized zirconia aerogel for high-performance thermal barrier coating. *J. Alloys Compd.* **2019**, *806*, 1430–1434. [[CrossRef](#)]
24. Zhang, M.; Wang, X.N.; Zhu, G.J.; Chen, C.J.; Hou, J.X.; Zhang, S.H.; Jing, H.M. Effect of Laser Welding Process Parameters on Microstructure and Mechanical Properties on Butt Joint of New Hot-Rolled Nano-scale Precipitation-Strengthened Steel. *Acta Metall. Sin-Engl.* **2014**, *27*, 521–529. [[CrossRef](#)]
25. Chen, J.; Li, C.S.; Ren, J.Y.; Tu, X.Y.; Cao, Y. Evaluation of microstructure and mechanical properties of Fe-1.2Mn-0.3Cr-1.4Ni-0.4Mo-C steel welded joints. *J. Mater. Res. Technol.* **2020**, *9*, 13793–13800. [[CrossRef](#)]
26. Li, Z.X.; Chen, J.S.; Wang, X.N.; Shen, X.J.; Cen, Y.M.; Chen, J.; Chu, Y.J.; Han, Y.J. Microstructure distribution and bending fracture mechanism of 65Mn steel in the laser surface treatment. *Mater. Sci. Eng. A* **2022**, *850*, 143568. [[CrossRef](#)]
27. Findley, K.O.; Hidalgo, J.; Huizenga, R.M.; Santofimia, M.J. Controlling the work hardening of martensite to increase the strength/ductility balance in quenched and partitioned steels. *Mater. Des.* **2017**, *117*, 248–256. [[CrossRef](#)]
28. Wang, P.F.; Chen, J.; Sun, B.T.; Zhu, D.H.; Cao, Y. Effects of annealing process parameters on microstructural evolution and strength-ductility combination of CoCrFeMnNi high-entropy alloy. *Mater. Sci. Eng. A* **2022**, *840*, 142880. [[CrossRef](#)]
29. Huang, X.X.; Hansen, N.; Tsuji, N. Hardening by annealing and softening by deformation in nanostructured metals. *Science* **2006**, *312*, 249–251. [[CrossRef](#)]
30. Yang, P.J.; Li, Q.J.; Han, W.Z.; Li, J.; Ma, E. Designing solid solution hardening to retain uniform ductility while quadrupling yield strength. *Acta Mater.* **2019**, *179*, 107–118. [[CrossRef](#)]
31. Wu, X.L.; Yang, M.X.; Yuan, F.P.; Wu, G.L.; Wei, Y.J.; Huang, X.X.; Zhu, Y.T. Heterogeneous lamella structure unites ultrafine-grain strength with coarse-grain ductility. *Proc. Natl. Acad. Sci. USA* **2015**, *112*, 14501–14505. [[CrossRef](#)] [[PubMed](#)]
32. Wu, X.L.; Zhu, Y.T. Heterogeneous materials: A new class of materials with unprecedented mechanical properties. *Mater. Res. Lett.* **2017**, *5*, 527–532. [[CrossRef](#)]
33. Zhu, Y.T.; Wu, X.L. Perspective on hetero-deformation induced (HDI) hardening and back stress. *Mater. Res. Lett.* **2019**, *7*, 393–398. [[CrossRef](#)]
34. Chen, X.; Zhang, B.X.; Zou, Q.; Huang, G.S.; Liu, S.S.; Zhang, J.L.; Tang, A.T.; Jiang, B.; Pan, F.S. Design of pure aluminum laminates with heterostructures for extraordinary strength-ductility synergy. *J. Mater. Sci. Technol.* **2022**, *100*, 193–205. [[CrossRef](#)]
35. Calcagnotto, M.; Ponge, D.; Demir, E.; Raabe, D. Orientation gradients and geometrically necessary dislocations in ultrafine grained dual-phase steels studied by 2D and 3D EBSD. *Mater. Sci. Eng. A* **2010**, *527*, 2738–2746. [[CrossRef](#)]
36. Liu, S.S.; Liu, H.; Chen, X.; Huang, G.S.; Zou, Q.; Tang, A.T.; Jiang, B.; Zhu, Y.T.; Pan, F.S. Effect of texture on deformation behavior of heterogeneous Mg-13Gd alloy with strength-ductility synergy. *J. Mater. Sci. Technol.* **2022**, *133*, 271–286. [[CrossRef](#)]
37. Zhu, Y.T.; Ameyama, K.; Anderson, P.M.; Beyerlein, I.J.; Gao, H.J.; Kim, H.S.; Lavernia, E.; Mathaudhu, S.; Mughrabi, H.; Ritchie, R.O.; et al. Heterostructured materials: Superior properties from hetero-zone interaction. *Mater. Res. Lett.* **2021**, *9*, 1–31. [[CrossRef](#)]
38. Li, X.F.; Nakatani, M.; Yang, J.R.; Zhang, J.X.; Sharma, B.; Pan, H.J.; Ameyama, K.; Fang, J.Q.; Zhu, X.K. Investigation of mechanical properties and microstructural evolution in Cu-Al alloys with gradient structure. *J. Alloys Compd.* **2022**, *890*, 161835. [[CrossRef](#)]
39. Wan, T.; Cheng, Z.; Bu, L.F.; Lu, L. Work hardening discrepancy designing to strengthening gradient nanotwinned Cu. *Scr. Mater.* **2021**, *201*, 113975. [[CrossRef](#)]
40. Zhang, B.H.; Chen, J.; Wang, P.F.; Sun, B.T.; Cao, Y. Enhanced strength-ductility of CoCrFeMnNi high-entropy alloy with inverse gradient-grained structure prepared by laser surface heat-treatment technique. *J. Mater. Sci. Technol.* **2022**, *111*, 111–119. [[CrossRef](#)]

Disclaimer/Publisher’s Note: The statements, opinions and data contained in all publications are solely those of the individual author(s) and contributor(s) and not of MDPI and/or the editor(s). MDPI and/or the editor(s) disclaim responsibility for any injury to people or property resulting from any ideas, methods, instructions or products referred to in the content.